Modeling the behavior of a drop on a superhydrophobic sheet

Erez Intrater, Yuri Feldman, and Oz Oshri*
Department of Mechanical Engineering, Ben-Gurion University of the Negev, Beer-Sheva 84105, Israel

(Received 12 August 2024; accepted 9 December 2024; published 13 January 2025)

The interaction between thin sheets and fluid droplets has recently attracted attention due to its frequent occurrence in natural systems and extensive use in technological applications. Motivated by these applications, this paper focuses on the interaction resulting from a drop that rests at the center of a circular superhydrophobic thin sheet. We investigate how the size and surface tension of the drop, together with the elastic and geometric parameters of the sheet, determine the overall deformation of the system. To this end, we formulate an analytical model based on energetic considerations that can predict the mutual interaction between the drop and the sheet. We show that the deformation of the sheet outside the contact region is almost unaffected by the exact shape of the drop, and thus mimics the problem of a rigid indentation. However, inside the contact region, there is a strong coupling between the drop's shape and the sheet's deformation. We derive analytical predictions for the size of the contact region and show that its shape comprises a constant curvature. These findings are in good quantitative agreement with the numerical minimization of the energy.

DOI: 10.1103/PhysRevE.111.015501

I. INTRODUCTION

Superhydrophobic surfaces—known for their exceptional water repellence—are exemplified by natural phenomena such as the self-cleaning properties of the lotus leaves [1,2] and the water-repellent wings of certain insects [3]. In technological applications, these surfaces are utilized in such diverse developments as water-resistant clothing [4], nonstick coatings [5], anti-icing surfaces for aviation [6], and enhanced fluid transport in microfluidic devices [7]. For further development of technological applications, the integration of superhydrophobicity into ultrathin surfaces would offer significant benefits by merging the unique fluid-repellent properties of superhydrophobic surfaces with the pliability of ultrathin materials. Much attention has recently been given to the mechanical behavior of ultrathin sheets, which possess nanoscale thickness and a remarkably high ratio of stretching to bending modulus. This mechanical flexibility allows ultrathin sheets to respond sensitively to minute external forces, such as those applied by a fluid drop. Drop-sheet interactions lead to phenomena such as capillary wrinkling of floating polymer films [8,9], droplets wrapping by thin sheets [10–12], snap-through of small beams under the influence of water drops [13], and large deformation of membranes due to static contact with drops [14–16]. The development of superhydrophobic ultrathin surfaces could be useful, for example, in the field of stretchable electronics [17,18], where ultrathin superhydrophobic layers protect sensitive components from moisture while maintaining the material's flexibility. Another potential application may be found in medical devices, where these surfaces could create coatings for implants or wearable devices [19,20].

Previous studies that investigated the interactions between droplets and superhydrophobic thin sheets have focused, for example, on the splashing of the drop from the sheet [21–23], and the enhancement of superhydrophobicity through substrate flexibility [24]. However, less attention has been given to the somewhat more basic problem that accounts for the static interaction of droplets with ultrathin superhydrophobic sheets. Therefore, in this paper we investigate the deformation resulting from an incompressible drop resting on top of a circular superhydrophobic thin sheet. Based on the weight and surface tension of the drop, as well as the mechanical and geometrical properties of the sheet, we formulate an analytical model that predicts the spatial deviations of the drop from its spherical shape and the accompanying deformations induced by the drop on the sheet.

The total energy of the system consists of the surface and gravitational energies of the drop, as previously considered in Ref. [25], and also of the elastic energy of the sheet. This elastic energy is accounted for in the membrane limit, where bending occurs at a zero energetic cost. This energetic formulation implies that the evolution of the system is governed by four dimensionless parameters: the Bond number $\mathbb{B}_o$, which accounts for the ratio between gravity and surface tension; the stretching capillary number Y_γ, which accounts for the ratio between the two-dimensional stretching modulus of the sheet and the surface tension of the drop; the normalized radius of the circular sheet R_{sh} (with all lengths normalized to the undeformed radius of the drop); and the Poisson's ratio of the sheet.

Since minimization of the total energy generally yields nonlinear and intractable equations, we first seek a direct solution to these equations only numerically. We then compare the numerical results with an approximated analytical solution that is derived based on three complementary assumptions. The first assumption is that the deflections are shallow, i.e.,

*Contact author: oshrioz@bgu.ac.il

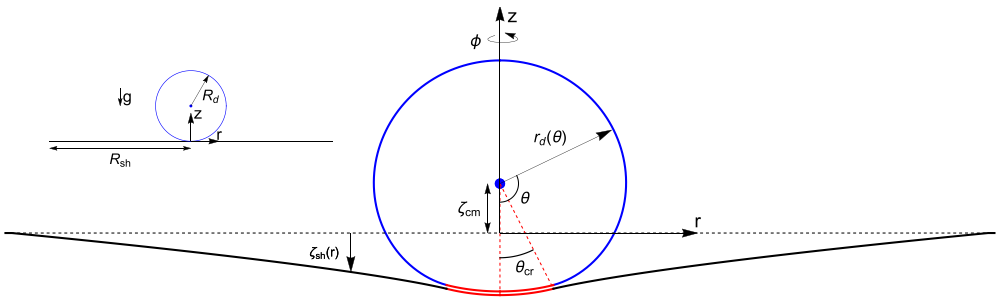

FIG. 1. Schematic overview of the system. A drop of undeformed radius R_d is placed at the center of a circular thin sheet with a rest radius R_{sh} (shown in the inset). The vertical deflection of the sheet is denoted by $\zeta_{sh}(r)$, where a cylindrical coordinate system is placed at the center of the undeformed sheet. The deformed configuration of the drop is described by the height ζ_{cm} of the center of mass of the drop above the relaxed configuration of the sheet, and the radius $r_d(\theta)$. The contact area between the sheet and the drop is denoted by the red part of the solid line, and θ_{cr} corresponds to the critical angle at which the detachment occurs.

that the drop does not deviate significantly from its undistorted spherical shape [25] and that the sheet deforms only within the small-slope approximation [26]. The second assumption, based on observations from the numerical solution, is that the configuration of the sheet consists of a spherical core region, where the drop and the sheet are in contact, and an outer region whose height decays to zero as a power law. The third assumption is that the deformation in the core region is localized, in the sense that the characteristics of this region are, to leading order, independent of the outer radius of the sheet.

Taken together, these assumptions allow us to derive approximate analytical solutions for the deflection of the sheet and the size and the shape of the core region. We show, for example, that the deflection of the sheet outside the contact region scales as $(\mathbb{B}_o R_{sh}^2/Y_\gamma)^{1/3}$, which implies that the weight of the drop is related to the cubic power of the deflection of the sheet, as seen in classical problems of indentation [27,28]. The radius of the contact area between the sheet and the drop deviates from that expected on a rigid surface by $Y_\gamma^{1/3}$. In addition, we show that the curvature of the sheet and its deflection in the core region cannot be described by simple scaling laws of the parameters Y_γ and $\mathbb{B}_o$.

The paper is organized as follows. In Sec. II, we formulate the problem and derive an expression for the total energy as a function of the deformation of the drop and the sheet. In Sec. III, we obtain an approximated solution to the problem. This analytical solution is then compared with the numerical minimization of the nonlinear energy in Sec. IV. Finally, in Sec.V, we summarize our main results and discuss possible extensions for future studies.

II. FORMULATION OF THE PROBLEM

We consider a circular thin sheet of radius R_{sh}, thickness h, Young's modulus e, and Poisson's ratio ν. A drop of an incompressible fluid with density ρ_d, surface tension γ, and total volume $V = 4\pi R_d^3/3$ is placed at the center of the sheet and is subjected to gravitational acceleration g. A system of cylindrical coordinates is placed at the center of the undeformed sheet (Fig. 1). We use the following assumptions to model the system: (i) the final configuration of the sheet and the drop has rotational symmetry around the z axis and (ii) the sheet, having a superhydrophobic surface, remains separated from the drop by a thin layer of gas.

Given the physical parameters of the sheet and the drop, we seek to determine the final configuration of the system, including, *inter alia*, the size of the contact area at the sheet-fluid interface, the maximum deflection of the sheet, and the deformations of the sheet and the drop.

The configuration of the sheet is described by the position vector

$$\mathbf{f}_{sh}(r,\phi) = [r + u_r(r)]\hat{\mathbf{r}}(\phi) + \zeta_{sh}(r)\hat{\mathbf{z}}, \tag{1}$$

where (r,ϕ) are the radial and the azimuthal coordinates that are attached to the undeformed configuration of the sheet, $u_r(r)$ and $\zeta_{sh}(r)$ are the components of the elastic displacement vector in the radial and the vertical directions, and the unit vectors $\hat{\mathbf{r}}(\phi)$ and $\hat{\mathbf{z}}$ are oriented along the r and the z directions, respectively. Since the sheet is clamped at the outer edge, and the radial displacement must vanish at the origin, we set the following boundary conditions on the displacements:

$$u_r(0) = 0 \quad \text{and} \quad u_r(R_{sh}) = \zeta_{sh}(R_{sh}) = 0. \tag{2}$$

The surface of the drop is described by

$$\mathbf{f}_d(\theta,\phi) = r_d(\theta)\sin\theta\hat{\mathbf{r}}(\phi) + [\zeta_{cm} - r_d(\theta)\cos\theta]\hat{\mathbf{z}}, \tag{3}$$

where ζ_{cm} is the height of the drop's center of mass above the relaxed configuration of the sheet, and $r_d(\theta)$ is a radial coordinate to the drop's contour, measured relative to the drop's center of mass.

Seemingly, to determine the configurations of the sheet and the drop, we need to specify the three functions $u_r(r)$, $\zeta_{sh}(r)$, and $r_d(\theta)$, and the parameter ζ_{cm}. However, along the contact area these functions are not independent but satisfy the relation $\mathbf{f}_{sh}(r,\phi) = \mathbf{f}_d(\theta,\phi)$. To characterize these constraints, we first define the parameters r_{cr} and θ_{cr} as the critical radius and the critical angle at which the sheet and the drop separate; see Fig. 1. These parameters are not yet known and must be determined from the solution. Second, we equate the components of the position vectors in the radial and the vertical directions; this gives

$$r \leqslant r_{cr}\ (\theta \leqslant \theta_{cr}): \quad r + u_r(r) = r_d\sin\theta, \tag{4a}$$

$$\zeta_{sh}(r) = \zeta_{cm} - r_d\cos\theta. \tag{4b}$$

In addition to these constraints along the contact area, we also need to account for two global constraints. One is that the total volume of the drop is conserved, and second is that $r_{\rm d}(\theta)$ is defined relative to the drop's center of mass. These constraints are given, respectively, by [29]

$$V = \frac{2\pi}{3}\int_0^\pi r_{\rm d}^3 \sin\theta d\theta, \tag{5a}$$

$$0 = \int_0^\pi r_{\rm d}^4 \sin(2\theta) d\theta. \tag{5b}$$

The total energy of the system comprises two contributions, $E = E_{\rm d} + E_{\rm sh}$, where $E_{\rm d}$ accounts for the gravitational energy of the drop and the energy associated with its surface tension, and $E_{\rm sh}$ accounts for the stretching energy of the sheet. Here we assume that the sheet is very thin, such that its bending energy is negligible compared to its stretching energy, which is the so-called membrane limit. The limits of validity of this assumption are discussed, for example, in Refs. [28,30] and Appendix D of Ref. [31]. This assumption asserts that the forces associated with bending are much smaller than those associated with the stretching of the sheet. Additionally, the length over which a torque relaxes in the membrane must be much smaller than the size of the contact length between the sheet and the drop.

In the following analysis, we normalize all lengths by the undeformed radius of the drop $R_{\rm d}$, and the energy, by $4\pi R_{\rm d}^2\gamma/3$. With these normalizations, the total energy of the system is given by

$$E = \mathbb{B}o\zeta_{\rm cm} + \frac{3}{2}\int_0^\pi \left((\partial_\theta r_{\rm d})^2 + r_{\rm d}^2\right)^{1/2} r_{\rm d}\sin\theta d\theta + \frac{3Y_\gamma}{4}\int_0^{R_{\rm sh}} (\sigma_{rr}\epsilon_{rr} + \sigma_{\phi\phi}\epsilon_{\phi\phi}) r dr, \tag{6}$$

where the first two terms correspond to the gravitational and surface energies of the drop, and the last term to the elastic energy of the sheet. In addition, we define the two dimensionless parameters,

$$\mathbb{B}_o = \frac{g\rho_{\rm d}R_{\rm d}^2}{\gamma} \quad \text{and} \quad Y_\gamma = \frac{eh}{\gamma(1-\nu^2)}, \tag{7}$$

that account, respectively, for the Bond number $\mathbb{B}_o$, i.e., the ratio of gravity to the surface tension, and the stretching capillary ratio [9], namely, the ratio between the two-dimensional stretching modulus of the sheet and the surface tension of the drop. As the Bond number increases, the impact of gravity on the deformation of the drop and on the deflection of the sheet increases. When Y_γ increases, the sheet becomes stiffer and harder to deflect. The limit of a rigid surface corresponds to $Y_\gamma \to \infty$, and is discussed, for example, in Ref. [25]. These two dimensionless numbers, in addition to the normalized radius of the sheet $R_{\rm sh}$ and Poisson's ratio ν, are the four independent parameters that completely characterize the problem. Furthermore, $\sigma_{\alpha\beta}$ and $\epsilon_{\alpha\beta}$ $(\alpha, \beta = r, \theta)$ correspond, respectively, to the normalized stresses and the strains in the sheet. Hereafter, we assume that the stress-strain relations follow Hooke's law, i.e., $\sigma_{rr} = \epsilon_{rr} + \nu\epsilon_{\phi\phi}$ and $\sigma_{\phi\phi} = \epsilon_{\phi\phi} + \nu\epsilon_{rr}$, and that strain-displacement relations are given by the Föppl–von Kármán theory [26]:

$$\epsilon_{rr} = \partial_r u_r + \frac{1}{2}(\partial_r \zeta_{\rm sh})^2, \quad \epsilon_{\phi\phi} = \frac{u_r}{r}. \tag{8}$$

This completes the formulation of the problem. In summary, given the four parameters $\mathbb{B}_o$, Y_γ, $R_{\rm sh}$, and ν, the equilibrium configuration of the system is determined by the minimization of the total energy, Eq. (6), with respect to the configuration of the drop, i.e., the parameter $\zeta_{\rm cm}$ and $r_{\rm d}(\theta)$, and the configuration of the sheet, $u_r(r)$ and $\zeta_{\rm sh}(r)$, under the constraints in the contact area, Eq. (4), and the constraints over the volume and the center of mass of the drop, Eq. (5). This direction for obtaining the equilibrium configuration yields, in general, a nonlinear and intractable set of equations. For this reason, we pursue this direction only numerically; see the numerical procedure in Appendix A. Nonetheless, using some insights from the numerical results, we are able to predict an approximated solution to the problem in the limit of shallow deflections. This direction for the solution is explained in the next section.

III. AN APPROXIMATED SOLUTION IN THE LIMIT OF SHALLOW DEFLECTIONS

In this section, we aim to find an approximated solution to the model by assuming that the contour of the drop is distorted only slightly from a spherical shape, and the sheet accommodates only shallow deflections. To this end, we follow Ref. [25] and assume that the normalized radius of the drop equals one, i.e., the drop is spherical, up to small changes that depend on the angle θ,

$$r_{\rm d}(\theta) = 1 + f(\theta), \tag{9}$$

where $f(\theta) \ll 1$ is an as-yet unknown function that describes small local deviations from the spherical shape. In the contact area, a normal force acts between the sheet and the drop, which generally has a nonzero projection in both the radial and vertical directions. However, for shallow deflections of the sheet, the normal force is oriented primarily in the z direction, and therefore we neglect the radial projection of this force. In our formulation, this requires us to neglect $u_r(r)$ in the constraint of the radial position vector, Eq. (4a). Additionally, we assume that the contact area between the sheet and the drop remains small, such that $\theta_{\rm cr} \ll 1$. Therefore, we assume hereafter that $r \simeq \theta$ inside the contact region.

The results of our numerical simulations consistently imply that the contact area between the sheet and the drop has a spherical shape. In addition, the height function of the sheet outside the critical region exhibits a power-law dependence on the radial coordinate. Taking into consideration the clamped boundary conditions at $R_{\rm sh}$, we set the following ansatz for the height of the sheet:

$$0 < r < r_{\rm cr}: \quad \zeta_{\rm sh}(r) = \zeta_0 + \frac{r^2}{2R}, \tag{10a}$$

$$r_{\rm cr} < r < R_{\rm sh}: \quad \zeta_{\rm sh}(r) = -\delta\left[1 - \left(\frac{r}{R_{\rm sh}}\right)^{2/3}\right], \tag{10b}$$

where ζ_0 represents the deflection of the sheet at $r = 0$ and corresponds to its maximum deflection, R denotes the radius

of curvature in the contact region, and δ is an arbitrary constant that remains to be determined. We can relate ζ_0 and R to the parameters δ and the critical radius $r_{\rm cr}$ using the continuity of the sheet at the take-off point, i.e., $\zeta_{\rm sh}(r)$ and its first derivative are continuous at $r_{\rm cr}$. This gives

$$\zeta_0 = \zeta_{\rm sh}(r_{\rm cr}) - \frac{\delta}{3}\left(\frac{r_{\rm cr}}{R_{\rm sh}}\right)^{2/3}, \quad R = \frac{3R_{\rm sh}^2}{2\delta}\left(\frac{r_{\rm cr}}{R_{\rm sh}}\right)^{4/3}. \tag{11}$$

In Eq. (10b), we choose a power of 2/3 to characterize the decay of the elastic shape. The rationale for this particular selection is that under a unique value of Poisson's ratio, this shape coincides with the exact solution of a sheet that is subjected to a point force [32]. In the next section, we show that deviations from this power do not considerably alter the leading order of the solution (although they do appear in the numerical data).

Under these approximations, our problem reduces to the one solved in Ref. [25], where a drop is considered to be resting on a rigid surface with a given constant curvature. The difference between the two problems lies in the fact that, in our case, the curvature of the surface is initially unknown and will be determined by the interaction of the drop with the sheet. As a result, we can adopt the solution obtained in Ref. [25] for the configuration of the drop, leaving R as an unknown parameter. This configuration is given by

$$\theta < \theta_{\rm cr}: \quad f(\theta) = \frac{c_1 - (1-\cos\theta)/R}{\cos\theta} - 1, \tag{12a}$$

$$\theta > \theta_{\rm cr}: \quad f(\theta) = c_2\left[\frac{\cos\theta}{3}\ln\left(\frac{1-\cos\theta}{2}\right) + \frac{1}{6} + \frac{4}{9}\cos\theta\right], \tag{12b}$$

where inside the contact region ($\theta < \theta_{\rm cr}$) the drop adopts the same shape as that of the sheet, and outside the contact region the configuration is determined by the minimization of the drop's energy under the global constraints, Eq. (5). This solution holds only up to quadratic order in $\theta_{\rm cr}^2$; see Ref. [25] for the details of this minimization. The constants c_1 and c_2 in this solution are determined so as to satisfy the continuity of the drop's contour and the contour's derivative across the critical angle $\theta_{\rm cr}$. For the sake of brevity, we do not explicitly present these constants herein.

Up to this point, we assumed an ansatz solution for the height function of the sheet that depends on the unknown parameters δ and $r_{\rm cr}$ (or $\theta_{\rm cr}$), and we obtained the drop's configuration as a function of these parameters. However, to calculate the energy, we still need to determine the radial displacement $u_r(r)$. Since the normal force that the drop exerts on the sheet acts, in our approximation, only in the z direction, we can readily minimize the elastic energy, i.e., the last term in Eq. (6), with respect to $u_r(r)$.

This minimization yields the force balance equation $\partial_r(r\sigma_{rr}) - \sigma_{\phi\phi} = 0$ [26], which must be satisfied inside and outside the contact region. Given the ansatz for the height's function, this equation results in a linear second-order equation for $u_r(r)$, which we need to solve using the boundary conditions of zero radial displacement at the origin and the outer radius, and continuous displacement and radial stress at the critical radius. While this problem is linear, and therefore analytically solvable, the solution is cumbersome, and so we do not write it here explicitly.

We can now substitute the elastic configuration, $u_r(r)$ and $\zeta_{\rm sh}(r)$, and the shape of the drop, $r_{\rm d}(\theta)$, into the energy, Eq. (6), and integrate over the spatial coordinates. By so doing, together with expanding the resulting expression to fourth order in $\theta_{\rm cr}$, similar to the order dictated by the solution for the drop's shape, and with neglecting terms of the order of $(r_{\rm cr}/R_{\rm sh})^{2/3}$ or higher, we obtain

$$\begin{aligned} E - E_0 = \mathbb{B}_o\Bigg[&-\delta + \frac{\theta_{\rm cr}^2}{2}\left(1-\frac{1}{R}\right)\left(\frac{5}{6} + 2\ln\left(\frac{\theta_{\rm cr}}{2}\right)\right)\Bigg] \\ &- \frac{\theta_{\rm cr}^4}{2}\left(1-\frac{1}{R}\right)^2\left[1 + \frac{3}{2}\ln\left(\frac{\theta_{\rm cr}}{2}\right)\right] \\ &+ \frac{Y_\gamma\delta^4(5-3\nu)(1+\nu)}{96R_{\rm sh}^2}, \end{aligned} \tag{13}$$

where $E_0 = 3 + \mathbb{B}_o$ is the normalized energy of a spherical drop that is in contact with the sheet only at its tip, as illustrated in the inset of Fig. 1. Equation (13) presents the explicit dependence of the energy on the variational parameters δ and $\theta_{\rm cr}$.

Minimization of the energy with respect to these parameters does still not yield tractable equations. To make further analytical progress, we note that previous studies that have considered the deflection of thin sheets by the application of localized forces ("indentation") have shown that the sheet's configuration outside the contact region depends very weakly on the minute details of the indenter [31,33]. For this reason, we choose to determine the parameter δ from the minimization of only two terms in the energy: the work that the drop's weight does on the outer region of the sheet and the elastic energy of the sheet [the first and last terms in Eq. (13)]. As a result, the parameters describing the exact shape of the drop, such as, for example, the critical radius, are not taken into consideration in determining δ. Minimization of these terms gives

$$\delta = \left(\frac{24}{(5-3\nu)(1+\nu)}\right)^{1/3}\left(\frac{\mathbb{B}_o R_{\rm sh}^2}{Y_\gamma}\right)^{1/3}. \tag{14}$$

Note that while the parameters $\mathbb{B}_o$ and Y_γ depend on γ, the ratio $\mathbb{B}_o/Y_\gamma$ is actually independent of surface tension. This independence of the solution on the surface energy of the drop signifies that in this approximation the sheet's deflection outside the contact region is independent of the drop's shape.

Given the approximated solution for δ, the energy now depends on a single parameter, $E = E(\theta_{\rm cr})$. However, the equation resulting from the minimization of the energy with respect to $\theta_{\rm cr}$ is not yet analytically solvable. We can derive an approximate solution for this angle by assuming a perturbative expansion in the inverse of the sheet stiffness, which is essentially equivalent to an expansion in powers of δ. To accomplish this expansion, we first minimize the energy [Eq. (13)] with respect to $\theta_{\rm cr}$. Then we expand the critical angle as $\theta_{\rm cr} = \theta_{\rm cr}^0 + \theta_{\rm cr}^1\delta + \ldots$, and solve the equation

perturbatively. To linear order, this gives the solution

$$\theta_{\rm cr} = \theta_{\rm cr}^{\rm rigid}\left(1 + \frac{3\sqrt[3]{2}(3 - \ln(36) + 2\ln \mathbb{B}_o)}{(11 - 2\ln(216) + 6\ln \mathbb{B}_o)(5 - 3\nu)^{1/3}(1+\nu)^{1/3}(\mathbb{B}_o Y_\gamma)^{1/3}}\right), \tag{15}$$

where $\theta_{\rm cr}^{\rm rigid} \equiv \sqrt{2\mathbb{B}_o/3}$ denotes the critical angle in the case of a rigid substrate ($Y_\gamma \to \infty$); see Ref. [25].

The solution given by Eqs. (14) and (15) is our central analytical result. It allows us to determine the configuration of the drop and the sheet given the parameters $\mathbb{B}_o$, Y_γ, $R_{\rm sh}$, and ν without any other fitting parameter. Interestingly, this approximated approach compares well with the numerical minimization of the nonlinear model, even beyond its strict limits. We present this comparison in the next section.

IV. RESULTS

This section is devoted to an investigation of the model's solution and is divided into two parts. In the first part, we focus on the solution outside the contact region. Since our system mimics the problem of a rigid indentation in this region [28], and since this problem has already been analyzed in several previous studies, we compare our approximated solution with known results from the literature. In the second part, we focus on the deformation inside the contact region and examine the dependence of $\theta_{\rm cr}$ and R on the drop's size and the stiffness of the surface.

A. Comparison with a rigid indenter

As a preliminary step to assess the validity of the approximated solution, we focus on the deformation of the system outside the contact area. We choose to do this because, in its simplest form, our problem consists of a circular sheet clamped at the outer edge and subjected to a local distribution of forces due to the drop's weight. Our analytical solution suggests that the exact distribution of these forces is immaterial because the parameter δ is independent of the surface tension of the drop and, consequently, of the exact shape of the drop. Therefore, we can directly compare our predictions with findings from prior studies that examined the shape of the sheet and the force-deflection relation in the case of a rigid indenter, where a force F in the z direction is assumed to act on the perimeter of a circle with radius $r_{\rm cr}$.

To devise our approximated approach to the case of the rigid indenter, it is instructive to first rewrite the ansatz of the height function, Eq. (10), in the following form:

$$\text{rigid indenter } (r_{\rm cr} < r < R_{\rm sh}):$$
$$\zeta_{\rm sh}(r) = -\bar{\delta}\frac{1 - \left(\frac{r}{R_{\rm sh}}\right)^{2/3}}{1 - \left(\frac{r_{\rm cr}}{R_{\rm sh}}\right)^{2/3}}. \tag{16}$$

With this modification, the height of the indenter at $r_{\rm cr}$ is given by $\bar{\delta} = \delta[1 - (r_{\rm cr}/R_{\rm sh})^{2/3}]$, where δ is given by Eq. (14). In the limit of a point indenter, i.e., an indenter with a vanishingly small radius, $\bar{\delta}$ coincides with δ. The total force that the drop exerts on the sheet equals its weight $F = 4\pi R_{\rm d}^3 g\rho_{\rm d}/3$. Therefore, by using Eq. (14), and when dimensions are restored in the model, we arrive at the following force-deflection relation:

$$\text{dimensional form:} \quad \frac{F}{ehR_{\rm sh}} = \alpha(\nu)\frac{\bar{\delta}^3}{R_{\rm sh}^3}, \quad \alpha(\nu) = \frac{\pi(5-3\nu)}{18(1-\nu)[1-(r_{\rm cr}/R_{\rm sh})^{2/3}]^3}. \tag{17}$$

Equation (17) recovers the well-known force-deflection relation for a vanishingly small prestretch $F \propto \bar{\delta}^3$, which has been verified in numerous experimental, numerical, and theoretical investigations; see, for example, Refs. [27,28,30–35] and references therein. In addition, for $\nu = 1/3$, the proportionality constant reduces to $\alpha(1/3) = (\pi/3)[1 - (r_{\rm cr}/R_{\rm sh})^{2/3}]^{-3}$, as obtained in the exact solution to this problem originally derived by Schwerin [32]. We note that this agreement with Schwerin's solution is obtained because for $\nu = 1/3$ the ansatz of the height function coincides with the exact solution of the equilibrium equations; see Appendix B for details.

We can further compare our approximated solution with the numerical solution of the rigid indenter equations for Poisson's ratios that differ from 1/3. These equations are given, for example, in Ref. [31], and for completeness, we repeat them in Appendix B. This comparison is presented in Fig. 2, where we plot the prefactor $\alpha(\nu)$ of the two solutions in panel (a) and examine the sheet's configurations in panel (b). Evidently, the two comparisons are in good agreement even for relatively large radii of the indenter. Nonetheless, some deviations occur when Poisson's ratio differs from 1/3, since, in this case, the ansatz deviates from the global energetic minimizer. Particularly, the deviations are most clearly seen in the deformation of the sheet, as the numerical solutions exhibit a decay power that significantly differs from 2/3. The numerical shapes have a power greater than 2/3 when $\nu < 1/3$ and smaller than 2/3 when $\nu > 1/3$. To emphasize these deviations, we added dashed lines at $\nu = 0$ and $\nu = 1/2$ in Fig. 2(b), corresponding to the fitting function $\zeta_{\rm sh}(r) \propto 1 - (r/R_{\rm sh})^\beta$. We find that $\beta \simeq 0.77$ when $\nu = 0$ and $\beta \simeq 0.59$ when $\nu = 1/2$. However, these deviations seem to have only a minor effect on the total elastic energy.

It should be noted that Vella and Davidovitch [31] obtained an exact solution for the case of a point indenter and extended this solution to the case $r_{\rm cr}/R_{\rm sh} \ll 1$ by using regular perturbation theory. Therefore, the reader may wonder about the benefit of using our approximated results when such solutions to the problem are already known. Our answer to this question

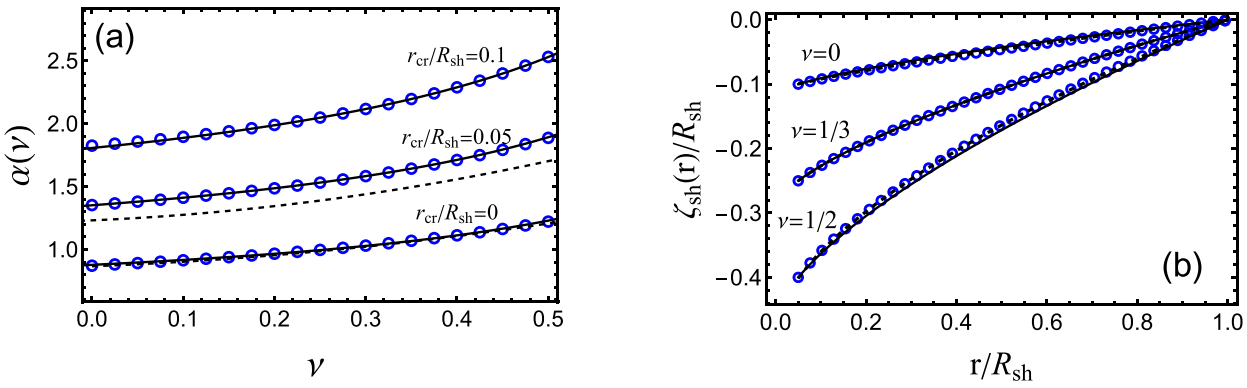

FIG. 2. Comparison between the numerical solution of the rigid indenter equations and the ansatz approach. In both panels, open blue circles represent the numerical solution of Eqs. (B2) and (B3), while solid black lines represent the ansatz approach. (a) The proportionality constant $\alpha(\nu)$ is shown for three different values of the indenter size. The ansatz solution is given by Eq. (17). The dashed line at $r_{cr}/R_{sh} = 0$ represents the exact solution for a point indenter (Eq. (47) in Ref. [31]). The dashed line below $r_{cr}/R_{sh} = 0.05$ corresponds to Eq. (48) from Ref. [31]. (b) The normalized height of the sheet is plotted as a function of r/R_{sh} for $r_{cr}/R_{sh} = 0.05$, and for three different values of the deflection: $\bar{\delta} = \{0.1, 0.25, 0.4\}R_{sh}$. The approximated solution is given by Eq. (16). The dashed lines represent the fitting function $\zeta_{sh} \propto 1 - (r/R_{sh})^{\beta}$, where $\beta \simeq 0.77$ when $\nu = 0$ and $\beta \simeq 0.59$ when $\nu = 1/2$.

is twofold. First, the exact solution of the problem is somewhat convoluted, since it requires a numerical solution of a transcendental equation. The solution of that equation yields the height function and the force-deflection relation in a parametric form, which does not immediately reveal the explicit dependence on Poisson's ratio. Therefore, our approach offers simplicity at some minor expense of accuracy. Second, the perturbative expansion around the exact solution provides a reasonable approximation of the force-deflection relation only in the limit $r_{cr}/R_{sh} \ll 1$, but fails to agree with the numerical solution at moderate values ($r_{cr}/R_{sh} \gtrsim 0.05$). For example, in Fig. 2(a) we plot the solution of the finite indenter given in Ref. [31] [dashed line, Eq. (48) in that paper] in comparison with our ansatz approach and the numerical data. We show that there are already relatively large discrepancies at $r_{cr}/R_{sh} = 0.05$. Therefore, our approach improves previous analytical predictions of a finite indenter.

To summarize, we demonstrate that our approximated solution outside the contact region aligns well with the existing model of a rigid indentation. With this in mind, we now proceed to analyze the deformation of the drop and the sheet in the core region, where the characteristics of the drop's shape have a substantial effect on the system's observables.

B. Deformation of the core region

As the size of the drop increases, its contour continuously deforms and tends to flatten against the underlying sheet, leading to an expansion of the contact area and an increase in the critical angle θ_{cr}. In Fig. 3(a), we plot this angle as a function of $\mathbb{B}_o$ for various values of the sheet's stiffness Y_γ, and compare the numerical solution of the nonlinear model [i.e., the minimization of Eq. (6)] with our approximated solution Eq. (15). Since a heavier drop has a larger contact area, the critical angle increases with the Bond number regardless of Y_γ. Additionally, for a given $\mathbb{B}_o$, the critical angle increases as the sheet becomes softer, because soft surfaces are more compliant and can better conform to the shape of the drop. For very high stiffness values, the solution no longer depends on the parameter Y_γ, and the critical angle converges to that expected on a rigid substrate, $\theta_{cr}^{rigid} \simeq (2\mathbb{B}_o/3)^{1/2}$ [dashed line in Fig. 3(a)].

We note that our numerical investigation focuses on a certain range of the stretching capillary parameter because typical experimental values of the two-dimensional stretching modulus of ultrathin sheets range between 0.1 N m^{-1} and 100 N m^{-1} [9,36]. Since the surface tension of a water drop is of the order of $\gamma \sim 0.1$ N m^{-1}, the stretching capillary parameter will range between $1 \lesssim Y_\gamma \lesssim 10^4$.

Interestingly, the agreement between the numerical and analytical solutions in Fig. 3(a) extends beyond the small δ limit assumed in our perturbative expansion of Eq. (15). It even fits well at moderate values of the critical angle $\theta_{cr} \lesssim 0.3$, which surpasses the small θ_{cr} assumption made earlier in our derivations. Deviations from the numerical data occur at relatively large Bond numbers ($\mathbb{B}_o \gtrsim 0.2$) and may be attributed primarily to deviation of the drop's contour from a spherical shape, and to the relatively small stiffness of the substrate when $Y_\gamma \sim O(1)$. Although one might expect the relative sizes of the contact region and the radius of the sheet to affect these deviations, we find that this ratio has only a minor effect on the fit to the numerical data. This insensitivity of θ_{cr} to the outer radius of the sheet is also evident in the analytical solution Eq. (15), which is independent of R_{sh}. This finding suggests that the deformation in the core region is localized, as mutual adjustments in the shapes of the sheet and drop within the contact region do not affect the deformation of the outer region.

Furthermore, changes in Poisson's ratio have a much smaller impact on the deformation of the contact region than on the force-deflection relation in the outer region. To illustrate the minor effects of changes in R_{sh} and ν on the solution of θ_{cr}, we added numerical data for $R_{sh} = 2$ and $\nu = 0$ to Fig. 3 (gray symbols). Clearly, these parameter changes modify the numerical solution only slightly. We can exploit this extended fitting of the analytical prediction to show that

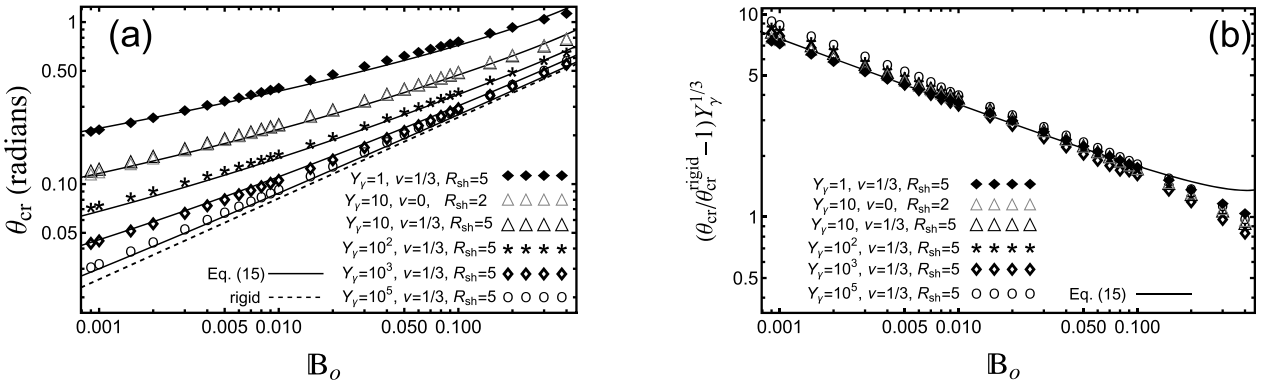

FIG. 3. The critical angle θ_{cr} as a function of $\mathbb{B}_o$. In both panels, symbols correspond to the numerical minimization of the total energy [Eq. (6)], and the solid black lines, to the analytical prediction of Eq. (15). (a) The critical angle as a function of $\mathbb{B}_o$ for several values of the sheet's stiffness. Dashed line corresponds to the analytical prediction on a rigid substrate $\theta_{cr}^{rigid} = \sqrt{2\mathbb{B}_o/3}$ [25]. (b) Collapse of the data presented in panel (a) into a single curve when the y axis is redefined to $(\theta_{cr}/\theta_{cr}^{rigid} - 1)Y_\gamma^{1/3}$. In the numerical analysis, the critical angle of a rigid surface is calculated by minimizing only the first two terms of Eq. (6) and by setting the sheet's radial displacement and height function to zero.

numerical data that is related to different sheet stiffnesses and to approximately different sheet sizes and Poisson's ratios collapse into a single curve when the y axis is redefined as $(\theta_{cr}/\theta_{cr}^{rigid} - 1)Y_\gamma^{1/3}$. In Fig. 3(b), this collapse is shown to hold for more than two orders of magnitude of the Bond number, and it essentially confirms the analytical prediction that the deviation of the critical angle from the rigid substrate solution scales as $Y_\gamma^{1/3}$.

The numerical data consistently imply that the drop and the sheet maintain a spherical geometry inside the contact region, as illustrated in Fig. 4, where the deformation of the sheet and the drop are plotted for several values of $\mathbb{B}_o$ and Y_γ. As the drop becomes heavier, i.e., Bond numbers increase, the deflection of the sheet increases, and the contact area increases. Additionally, on stiff sheets, the drop's contour appears to flatten against the underlying sheet as the $\mathbb{B}_o$ increases, while on very soft sheets, the drop remains nearly circular and the sheet tends to wrap around it. The analytical prediction, which assumes a parabolic shape within the contact region, matches well with the numerical configurations when $Y_\gamma \gtrsim 10$. However, significant discrepancies arise at the lowest sheet stiffness, even though the numerical contact area remains nearly spherical. In any case, the curvature of this region, $1/R$, is yet another observable that we can measure numerically and compare to the analytical solution [Eq. (11)].

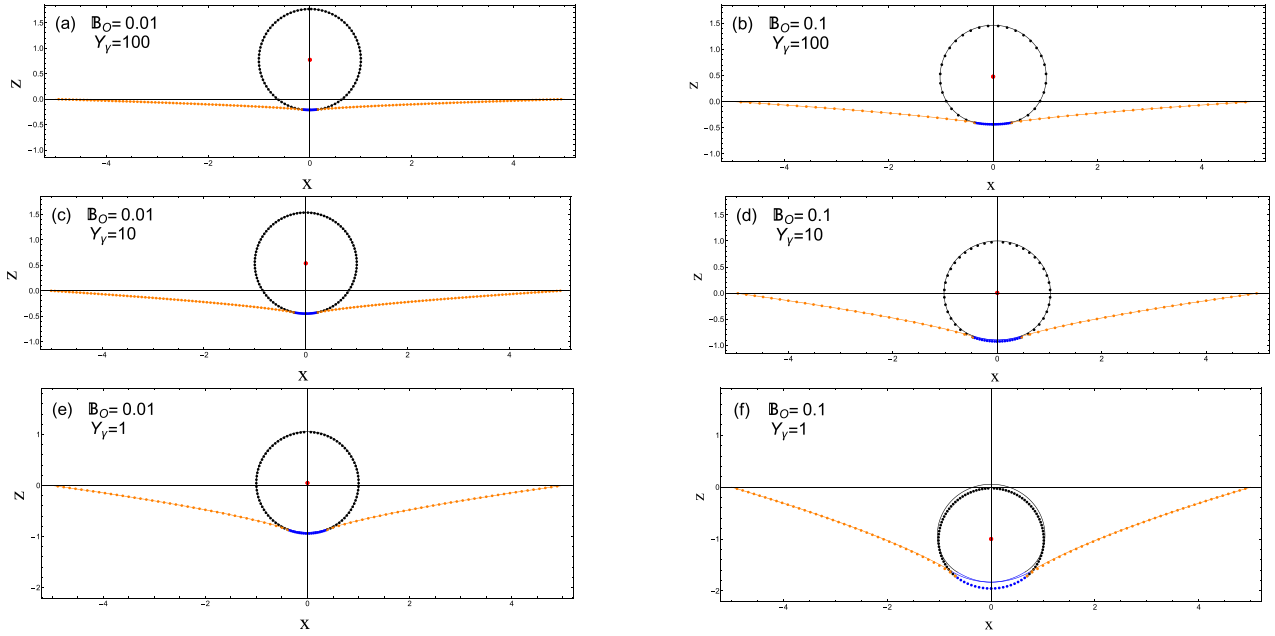

FIG. 4. Cross section of the system configuration for different Bond numbers $\mathbb{B}_o$ and sheet stiffnesses Y_γ. In all panels, dots represent the solution obtained from the numerical minimization of Eq. (6) with $R_{sh} = 5$ and $\nu = 1/3$, and solid lines represent the analytical predictions. The orange and the black colored parts of the sheet and the drop, respectively, correspond to the regions outside the contact area. The blue colored parts correspond to the contact region. The red dot indicates the center of mass of the drop ζ_{cm}.

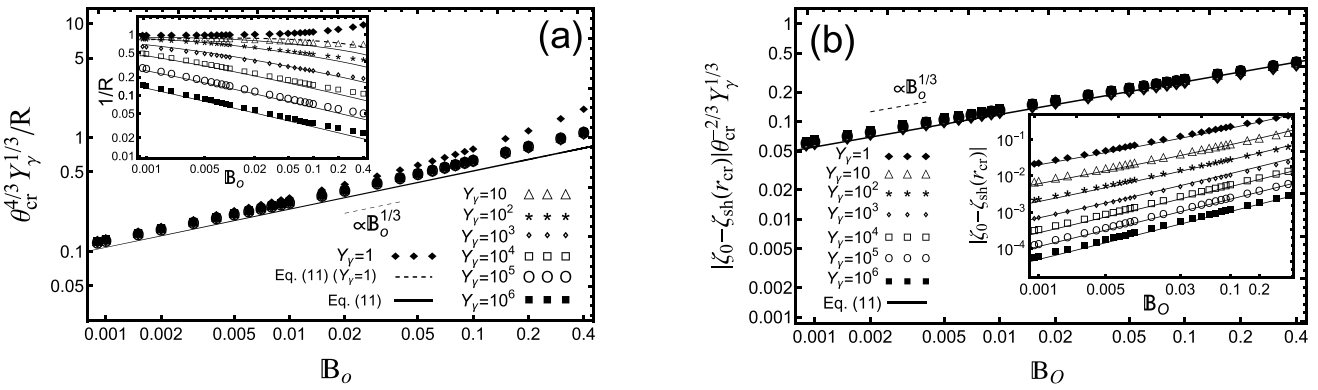

FIG. 5. The curvature and the deflection of the contact region. In both panels, symbols correspond to the numerical minimization of Eq. (6) with $R_{sh} = 5$ and $\nu = 1/3$, and solid lines to the analytical predictions Eq. (11). (a) The inset shows the curvature as a function of $\mathbb{B}_o$ for different values of Y_γ. The dashed line in the inset corresponds to Eq. (11) with $Y_\gamma = 1$. The data collapse into a single curve when the y axis is redefined to $\theta_{cr}^{4/3} Y_\gamma^{1/3}/R$, as shown in the main figure. (b) The inset shows the deflection of the sheet in the core region as a function of $\mathbb{B}_o$ for different sheet stiffnesses. All data collapse into a single curve when the y axis is redefined as $|\zeta_0 - \zeta_{sh}(r_{cr})|\theta_{cr}^{-2/3} Y_\gamma^{1/3}$.

The numerical data for this curvature and its comparison with the analytical prediction are plotted in the inset of Fig. 5. Since stiffer sheets are harder to deform, the curvature decreases as Y_γ increases. Additionally, as the drop becomes heavier, it tends to flatten against the sheet, thus increasing the radius of curvature. However, simultaneously, the sheet deflects and wraps around the drop, thereby acting to decrease the radius of curvature. Overall, for the stiff sheets ($Y_\gamma \gtrsim 10$), the balance between these two effects causes the curvature to decrease, indicating that the flattening of the drop has a greater influence than the wrapping of the sheet. However, for softer sheets ($Y_\gamma = 1$), the curvature increases, and the warping of the sheet has a greater effect than the flattening of the drop.

The analytical prediction captures this delicate balance only in part. For the case of stiff sheets ($Y_\gamma \gtrsim 10$), we find that the theory is within reasonable quantitative agreement with the numerical data; see the correspondence between the analytical and numerical data in the inset of Fig. 5(a). However, significant deviations occur at large $\mathbb{B}_o$ numbers, where the drop deviates from the spherical shape. Note that once δ from Eq. (14) is substituted into Eq. (11), the resulting analytical curvature becomes independent of the size of the sheet. Therefore, the analytical solution once again demonstrates the locality of the deformation in the core region. To further appreciate the analytical prediction, we note that numerical data corresponding to different sheet stiffnesses collapse into a single curve when the y axis is redefined as $\theta_{cr}^{4/3} Y_\gamma^{1/3}/R \propto \mathbb{B}_o^{1/3}$ (Fig. 5). This collapse demonstrates that the dependence of the curvature on Y_γ and $\mathbb{B}_o$ cannot be captured by a simple power law because the critical angle θ_{cr} depends on these parameter in a complex manner, as shown in Eq. (15).

While the behavior of stiff sheets is adequately described by the theory, large discrepancies are observed at lower values of the sheet stiffness ($Y_\gamma = 1$). In particular, in this case, our theory does not capture the increase in the curvature of the contact area [see the dashed line in the inset of Fig. 5(a)]. This discrepancy can be attributed to the fact that the theory is strictly valid for large values of Y_γ.

We complete this investigation by examining the deflection of the midpoint on the sheet, ζ_0. Equation (11) suggests that this deflection consists of two contributions: one from the deflection of the sheet at the critical radius, $\zeta_{sh}(r_{cr})$, and the other from the deflection of the core region relative to the height at r_{cr}. Since the first term has already been compared with previous results in Sec. IV A, we focus here on the deflection caused by the drop's shape inside the contact region.

In the inset of Fig. 5(b), we plot this correction, i.e., $|\zeta_0 - \zeta_{sh}(r_{cr})|$, as a function of $\mathbb{B}_o$ and for several values of Y_γ. As expected, the deflection increases with an increase in the size of the drop and decreases as the sheet becomes stiffer. The analytical prediction agrees well with the numerical data. To further demonstrate the strength of this analytical prediction, we note that all numerical data collapse into a single curve when the y axis is redefined to $|\zeta_0 - \zeta_{sh}(r_{cr})|\theta_{cr}^{-2/3} Y_\gamma^{1/3} \propto \mathbb{B}_o^{1/3}$, as shown in Fig. 5(b). As in the case of the curvature, this collapse emphasizes that the dependence of the core region on Y_γ is of a more complicated nature than can be described by a scaling law.

V. SUMMARY AND CONCLUDING REMARKS

We developed an analytical model to describe the static interaction between a drop and a circular superhydrophobic thin sheet. Our model minimizes an energy functional that takes into consideration the gravitational and surface energies of the drop and the elastic energy of the sheet. To investigate the equilibrium configurations of the system, we first developed a numerical scheme that allows us to obtain the global minimizer of the energy. Then we derived an analytical approximation for this minimizer by using the assumption of shallow deflections. We demonstrated that this approximation agrees well with the numerical data for large stiffness values of the sheet.

Our model makes several key predictions. First, the deformation of the system can be divided into two regions, namely, an external region, outside the contact area, where elastic deformations are largely independent of the exact shape of the drop, and an inner (core) region, where the deformations of the sheet and the drop are interrelated. This screening between the two regions likely results from our membrane limit

assumption, which implies that the sheet can change its curvature rapidly at a very small energetic cost. As a consequence of this localization, the deformation of the sheet outside the contact region is nearly independent of the precise distribution of the drop's weight, and the system exhibits behavior similar to that observed in the problem of a rigid indentation, namely, the total weight of the drop scales with the cubic power of the sheet's deflection.

In addition, we derived approximated solutions for the length [Eq. (15)], the curvature, and the deflection [Eq. (11)] of the contact region. To leading order, all these parameters are found to be independent of the outer radius of the sheet. For very stiff sheets ($Y_\gamma \gg 1$), the solution converges to that expected on a rigid substrate, where the curvature and the deflection approach zero and $\theta_{\rm cr}$ converges to $\theta_{\rm cr}^{\rm rigid}$ [25]. However, significant deviations from this rigid case are observed when the sheet's stiffness is relaxed. In that case, the deviation of the critical angle from the solution on a rigid surface scales as $Y_\gamma^{1/3}$. Additionally, we found that the contact region adopts a spherical shape for all sheet stiffnesses and Bond numbers that we examined. For relatively large Y_γ, the curvature of this spherical region decreases as $\mathbb{B}_o$ increases; however, the curvature increases for softer sheets.

While our study focuses only on the static interaction between the sheet and the drop, it can still serve as the base solution for more complex setups, such as vibrations of drops on thin sheets or the impact of viscous droplets with small Weber numbers on ultrathin sheets. Nonetheless, we note that the current analysis makes the somewhat constraining assumption that the sheet has zero prestretch, i.e., the boundary condition of the radial displacement at the outer radius is given by $u_r(R_{\rm sh}) = 0$. However, in most experimental setups, the sheet is not initially in a stress-free configuration but is subjected to some external tension ($u_r(R_{\rm sh}) > 0$). This pretension qualitatively affects the rigid indenter solution, for example, by adding a linear term to the force-deflection relation. Therefore, to make the current study more applicable for comparison with experimental data, it is necessary first to extend the formulation to include the case of a prestretched sheet.

ACKNOWLEDGMENT

This research was supported by the Israel Science Foundation (Grant No. 950/22).

APPENDIX A: NUMERICAL SCHEME FOR THE MINIMIZATION OF THE TOTAL ENERGY

In this appendix, we detail our numerical scheme for the minimization of the energy. We start by dividing the radius of the sheet into $N_{\rm sh}$ discrete points, where among these points, $N_{\rm cr}$ lie inside the contact region, i.e.,

$$r_i = \begin{cases} \frac{i r_{\rm cr}}{N_{\rm cr}-1}, & i = 0, \ldots, N_{\rm cr}-1 \\ r_{\rm cr} + \frac{i(R_{\rm sh}-r_{\rm cr})}{N_{\rm sh}-1}, & i = N_{\rm cr}, \ldots, N_{\rm sh}-1, \end{cases} \tag{A1}$$

where $r_{\rm cr} \equiv r_{N_{\rm cr}-1}$ is an as-yet unknown parameter. At each point along the sheet, we define the discrete elastic fields u_r^i and $\zeta_{\rm sh}^i$. The boundary conditions, Eq. (2), are accounted for by

$$u_r^1 = u_r^{N_{\rm sh}} = \zeta_{\rm sh}^{N_{\rm sh}} = 0. \tag{A2}$$

Similarly, the contour of the drop is divided into $N_{\rm d}$ points, where $N_{\rm cr}$ of these points lie inside the contact region. To discretize the angle θ along these points, we choose

$$\theta_i = \begin{cases} \sin^{-1}\left(\frac{r_i + u_r^i}{r_{\rm d}^i}\right), & i = 0, \ldots, N_{\rm cr}-1 \\ \theta_{\rm cr} + \frac{i(\pi-\theta_{\rm cr})}{N_{\rm d}-1}, & i = N_{\rm cr}, \ldots, N_{\rm d}-1, \end{cases} \tag{A3}$$

such that inside the contact region, the constraint Eq. (4a) is automatically satisfied. In addition, we denote the critical angle by $\theta_{\rm cr} = \theta_{N_{\rm cr}-1}$, and define the discrete radius of the drop $r_{\rm d}^i$ at each point θ_i.

Given the discretizations of the coordinates $\{r_i, \theta_i\}$, the elastic fields $\{u_r^i, \zeta_{\rm sh}^i\}$, and the drop's radius $\{r_{\rm d}^i\}$, we can now express the total energy [Eq. (6)] by using the following discrete summations:

$$\begin{aligned} E = {} & \mathbb{B}o\zeta_{\rm cm} + \frac{3}{2}\sum_{i=1}^{N_{\rm d}-1}\left[\left(\frac{r_{\rm d}^{i+1}-r_{\rm d}^i}{\theta_{i+1}-\theta_i}\right)^2 + \left(r_{\rm d}^{i+1/2}\right)^2\right]^{1/2} \\ & \times r_{\rm d}^{i+1/2}\sin(\theta_{i+1/2})\Delta\theta \\ & + \frac{3Y_\gamma}{4}\sum_{i=1}^{N_{\rm sh}-1}\left[\sigma_{rr}^{i+1/2}\epsilon_{rr}^{i+1/2} + \sigma_{\phi\phi}^{i+1/2}\epsilon_{\phi\phi}^{i+1/2}\right] r_{i+1/2}\Delta r, \end{aligned} \tag{A4}$$

where $\Delta\theta = \theta_{i+1} - \theta_i$ and $\Delta r = r_{i+1} - r_i$, and we use the notation $i+1/2$ to denote a midpoint of, for example, $r_{\rm d}^{i+1/2} = (r_{\rm d}^{i+1} + r_{\rm d}^i)/2$. In addition, the stress-strain relations are given by $\sigma_{rr}^{i+1/2} = \epsilon_{rr}^{i+1/2} + \nu\epsilon_{\phi\phi}^{i+1/2}$ and $\sigma_{\phi\phi}^{i+1/2} = \epsilon_{\phi\phi}^{i+1/2} + \nu\epsilon_{rr}^{i+1/2}$, and the strain-displacements relations are

$$\epsilon_{rr}^{i+1/2} = \frac{u_r^{i+1}-u_r^i}{r_{i+1}-r_i} + \frac{1}{2}\left(\frac{\zeta_{i+1}-\zeta_i}{r_{i+1}-r_i}\right)^2, \quad \epsilon_{\phi\phi}^{i+1/2} = \frac{u_r^{i+1/2}}{r_{i+1/2}}. \tag{A5}$$

The energy Eq. (A4) is minimized under the constraints Eqs. (4b) and (5). The discretizations of these equations are given by

$$\zeta_{\rm sh}^i = \zeta_{\rm cm} - r_{\rm d}^i\cos\theta_i, \tag{A6a}$$

$$V = \frac{2\pi}{3}\sum_{i=1}^{N_{\rm d}-1}\left(r_{\rm d}^{i+1/2}\right)^3\sin\theta_{i+1/2}\Delta\theta, \tag{A6b}$$

$$0 = \sum_{i=1}^{N_{\rm d}-1}\left(r_{\rm d}^{i+1/2}\right)^4\sin(2\theta_{i+1/2}), \tag{A6c}$$

where the normalized volume of the drop is $V = 4\pi/3$.

Overall, our numerical problem reduces to finding $2N_{\rm sh} + N_{\rm d} + 2$ unknown variables $\{u_r^i, \zeta_{\rm sh}^i, r_{\rm d}^i, \zeta_{\rm cm}, r_{\rm cr}\}$ from the minimization of the total energy Eq. (A4) under the constraints Eq. (A6). Given the parameters $\mathbb{B}o$, Y_γ, $R_{\rm sh}$, and ν, this constrained minimization is performed using the FindMinimum routine in Mathematica [37].

APPENDIX B: THE MODEL OF A RIGID INDENTER

In Sec. IV A, we compare some of our analytical results with those obtained from the model of a rigid indenter. For completeness, we repeat the main equations of this model here.

We consider an annular sheet with inner and outer radii $r_{\rm cr}$ and $R_{\rm sh}$, respectively, that is subjected to a force F acting in the z direction along the inner radius. The sheet is clamped at the outer radius. The elastic deformation is obtained from the minimization of the sheet's stretching energy and the work of the external force. This energy is given by

$$\text{rigid indenter:}\quad E=\frac{1}{2}\int_0^{2\pi}\int_{r_{\rm cr}}^{R_{\rm sh}}(\sigma_{rr}\epsilon_{rr}+\sigma_{\phi\phi}\epsilon_{\phi\phi})rdrd\theta+F\zeta_{\rm sh}(r_{\rm cr}), \tag{B1}$$

where stress-strain relations are assumed to follow Hook's law, and strain-displacement relations follow from the small-slope approximation, Eq. (8). Minimization of this energy with respect to the radial displacement of the sheet and its height function gives the following equations:

$$\partial_r(r\sigma_{rr})-\sigma_{\phi\phi}=0, \tag{B2a}$$

$$r\sigma_{rr}\partial_r\zeta_{\rm sh}=\frac{F}{2\pi}. \tag{B2b}$$

These equations are supplemented by the following boundary conditions:

$$u_r(r_{\rm cr})=u_r(R_{\rm sh})=\zeta_{\rm sh}(R_{\rm sh})=0. \tag{B3}$$

Given force F, we can now solve Eqs. (B2) and (B3) to obtain the sheet's deflection. An example of this solution is plotted in Fig. 2 in the main text (open blue circles). An analytical solution to these equations in the case where $r_{\rm cr}=0$ is given in Ref. [31] (Appendix B in that paper). In addition, in the case where $\nu=1/3$, the exact solution of Eq. (B2) is given by $u_r(r)=0$ and Eqs. (16) and (17) for the height function.

[1] C. Neinhuis and W. Barthlott, Characterization and distribution of water-repellent, self-cleaning plant surfaces, Ann. Bot. **79**, 667 (1997).

[2] A. Marmur, The lotus effect: Superhydrophobicity and metastability, Langmuir **20**, 3517 (2004).

[3] D. Byun, J. Hong, J. H. Ko, Y. J. Lee, H. C. Park, B.-K. Byun, and J. R. Lukes, Wetting characteristics of insect wing surfaces, J. Bionic Eng. **6**, 63 (2009).

[4] S. Park, J. Kim, and C. H. Park, Superhydrophobic textiles: Review of theoretical definitions, fabrication and functional evaluation, J. Eng. Fibers Fabr. **10** (2015).

[5] E. Bormashenko and Y. Bormashenko, Non-stick droplet surgery with a superhydrophobic scalpel, Langmuir **27**, 3266 (2011).

[6] C. Antonini, M. Innocenti, T. Horn, M. Marengo, and A. Amirfazli, Understanding the effect of superhydrophobic coatings on energy reduction in anti-icing systems, Cold Reg. Sci. Technol. **67**, 58 (2011).

[7] M. Elsharkawy, T. M. Schutzius, and C. M. Megaridis, Inkjet patterned superhydrophobic paper for open-air surface microfluidic devices, Lab Chip **14**, 1168 (2014).

[8] J. Huang, M. Juszkiewicz, W. H. de Jeu, E. Cerda, T. Emrick, N. Menon, and T. P. Russell, Capillary wrinkling of floating thin polymer films, Science **317**, 650 (2007).

[9] B. Davidovitch and D. Vella, Partial wetting of thin solid sheets under tension, Soft Matter **14**, 4913 (2018).

[10] C. Py, P. Reverdy, L. Doppler, J. Bico, B. Roman, and C. N. Baroud, Capillary origami: Spontaneous wrapping of a droplet with an elastic sheet, Phys. Rev. Lett. **98**, 156103 (2007).

[11] J. D. Paulsen, V. Démery, C. D. Santangelo, T. P. Russell, B. Davidovitch, and N. Menon, Optimal wrapping of liquid droplets with ultrathin sheets, Nat. Mater. **14**, 1206 (2015).

[12] A. Antkowiak, B. Audoly, C. Josserand, S. Neukirch, and M. Rivetti, Instant fabrication and selection of folded structures using drop impact, Proc. Natl. Acad. Sci. USA **108**, 10400 (2011).

[13] A. Fargette, S. Neukirch, and A. Antkowiak, Elastocapillary snapping: Capillarity induces snap-through instabilities in small elastic beams, Phys. Rev. Lett. **112**, 137802 (2014).

[14] V. Nair, I. Sharma, and V. Shankar, Planar equilibria of sessile and pendant liquid drops on geometrically non-linear elastic membranes, Phys. Fluids **30**, 082114 (2018).

[15] G. Kozyreff, B. Davidovitch, S. G. Prasath, G. Palumbo, and F. Brau, Effect of external tension on the wetting of an elastic sheet, Phys. Rev. E **107**, 035101 (2023).

[16] S. Neukirch, A. Antkowiak, and J.-J. Marigo, The bending of an elastic beam by a liquid drop: A variational approach, Proc. R. Soc. A **469**, 20130066 (2013).

[17] J. Dong, D. Wang, Y. Peng, C. Zhang, F. Lai, G. He, P. Ma, W. Dong, Y. Huang, I. P. Parkin, and T. Liu, Ultra-stretchable and superhydrophobic textile-based bioelectrodes for robust self-cleaning and personal health monitoring, Nano Energy **97**, 107160 (2022).

[18] J. A. Rogers, T. Someya, and Y. Huang, Materials and mechanics for stretchable electronics, Science **327**, 1603 (2010).

[19] Y. Lee and J.-H. Ahn, Biomimetic tactile sensors based on nanomaterials, ACS Nano **14**, 1220 (2020).

[20] K. Xu, Y. Lu, and K. Takei, Multifunctional skin-inspired flexible sensor systems for wearable electronics, Adv. Mater. Technol. **4**, 1800628 (2019).

[21] R. E. Pepper, L. Courbin, and H. A. Stone, Splashing on elastic membranes: The importance of early-time dynamics, Phys. Fluids **20**, 082103 (2008).

[22] G. Upadhyay, V. Kumar, and R. Bhardwaj, Bouncing droplets on an elastic, superhydrophobic cantilever beam, Phys. Fluids **33**, 042104 (2021).

[23] J.-H. Kim, J. P. Rothstein, and J. K. Shang, Dynamics of a flexible superhydrophobic surface during a drop impact, Phys. Fluids **30**, 072102 (2018).

[24] T. Vasileiou, J. Gerber, J. Prautzsch, T. M. Schutzius, and D. Poulikakos, Superhydrophobicity enhancement through substrate flexibility, Proc. Natl. Acad. Sci. USA **113**, 13307 (2016).

[25] J. Moláček and J. W. M. Bush, A quasi-static model of drop impact, Phys. Fluids **24**, 127103 (2012).

[26] L. D. Landau and E. M. Lifshitz, *Theory of Elasticity*, 3rd ed. (Butterworth-Heinemann, Oxford, 1986).

[27] C. Lee, X. Wei, J. W. Kysar, and J. Hone, Measurement of the elastic properties and intrinsic strength of monolayer graphene, Science **321**, 385 (2008).

[28] U. Komaragiri, M. R. Begley, and J. G. Simmonds, The mechanical response of freestanding circular elastic films under point and pressure loads, J. Appl. Mech. **72**, 203 (2005).

[29] To derive Eq. (5b) we first write $\zeta_{\rm cm} = \frac{1}{V}\int_0^{2\pi}\int_0^{\pi}\int_0^{r_{\rm d}}(\zeta_{\rm cm} - \tilde{r}_{\rm d}\cos\theta)\tilde{r}_{\rm d}^2\sin\theta d\tilde{r}_{\rm d}d\theta d\phi$, where V is the total volume of the drop and the integration is over this volume. Second, we perform the integration over the ϕ and the $\tilde{r}_{\rm d}$ coordinates. This gives the equation in the main text.

[30] M. R. Begley and T. J. Mackin, Spherical indentation of freestanding circular thin films in the membrane regime, J. Mech. Phys. Solids **52**, 2005 (2004).

[31] D. Vella and B. Davidovitch, Indentation metrology of clamped, ultra-thin elastic sheets, Soft Matter **13**, 2264 (2017).

[32] E. Schwerin, Über Spannungen und Formänderungen kreisringförmiger Membranen, Z. Angew. Math. Mech. **9**, 482 (1929).

[33] G. Alboteanu and A. Ya'akobovitz, Exceptionally large fracture strength and stretchability of 2D ReS^2 and $ReSe^2$, Nanoscale **16**, 3454 (2024).

[34] K.-T. Wan, S. Guo, and D. A. Dillard, A theoretical and numerical study of a thin clamped circular film under an external load in the presence of a tensile residual stress, Thin Solid Films **425**, 150 (2003).

[35] A. Falin, Q. Cai, E. J. Santos, D. Scullion, D. Qian, R. Zhang, Z. Yang, S. Huang, K. Watanabe, T. Taniguchi, M. R. Barnett, Y. Chen, R. S. Ruoff, and L. H. Li, Mechanical properties of atomically thin boron nitride and the role of interlayer interactions, Nat. Commun. **8**, 15815 (2017).

[36] D. Kumar, T. P. Russell, B. Davidovitch, and N. Menon, Stresses in thin sheets at fluid interfaces, Nat. Mater. **19**, 690 (2020).

[37] W. R. Inc., Mathematica, Version 12.3 (2018).